The Astrophysical Journal Supplement Series, 150:165–180, 2004 January

EMISSION LINE PROPERTIES OF ACTIVE GALACTIC NUCLEI FROM A POST-COSTAR *HUBBLE SPACE TELESCOPE* FAINT OBJECT SPECTROGRAPH SPECTRAL ATLAS

Joanna K. Kuraszkiewicz and Paul J. Green
Harvard-Smithsonian Center for Astrophysics, 60 Garden Street, Cambridge, MA 02138;
jkuraszkiewicz@cfa.harvard.edu, pgreen@cfa.harvard.edu

D. Michael Crenshaw and Jay Dunn
Department of Physics and Astronomy, Georgia State University, Astronomy Offices, One Park Place South SE, Suite 700, Atlanta, GA 30303; crenshaw@chara.gsu.edu, dunn@chara.gsu.edu

Karl Forster
California Institute of Technology, 1200 East California Boulevard, MC 405-47, Pasadena, CA 91125; krl@srl.caltech.edu

Marianne Vestergaard
Ohio State University, Columbus, 140 West 18th Avenue, Columbus, OH 43210; vester@astronomy.ohio-state.edu

and

Tom L. Aldcroft
Harvard-Smithsonian Center for Astrophysics, 60 Garden Street, Cambridge, MA 02138; taldcroft@cfa.harvard.edu
Received 2003 July 24; accepted 2003 September 12

ABSTRACT

We present consistent emission-line measurements for active galactic nuclei (AGNs), useful for reliable statistical studies of emission line properties. This paper joins a series including similar measurements of 993 spectra from the Large Bright Quasar Survey and 174 spectra of AGNs obtained from the Faint Object Spectrograph (FOS) on the *Hubble Space Telescope* (*HST*) prior to the installation of COSTAR. This time we concentrate on 220 spectra obtained with the FOS after the installation of COSTAR, completing the emission line analysis of all FOS archival spectra. We use the same automated technique as in previous papers, which accounts for Galactic extinction, models blended optical and UV iron emission, includes Galactic and intrinsic absorption lines, and models emission lines using multiple Gaussians. We present UV and optical emission line parameters (equivalent widths, fluxes, FWHM, and line positions) for a large number (28) of emission lines including upper limits for undetected lines. Further scientific analyses will be presented in subsequent papers.

Subject headings: atlases — galaxies: active — quasars: emission lines — quasars: general — ultraviolet: galaxies

On-line material: color figure, machine-readable tables

1. INTRODUCTION

It is broadly acknowledged that the quasar central engine (presumably a massive black hole with an accretion disk) photoionizes gas lying farther out. This gas emits broad permitted emission lines that are distinctive of quasar spectra. At first glance, quasar spectra look quite similar; this may be the result of simple averaging. Baldwin et al. (1995) showed that although the broad line region (BLR) consists of clouds with a wide range of properties (gas density, ionization flux, and column density), the bulk of emission line flux is most likely produced in the gas clouds with the optimum parameters for efficient emission in that line.

A closer look at the quasar spectra, however, reveals that the spectra differ in detail and, intriguingly, behave in a correlated manner. For example, it was found that active galactic nuclei (AGNs) that show strong optical iron emission (Fe II λ4570) have weaker [O III] λ5007, and narrower, blue-asymmetric Hβ lines. This set of correlations was found to be the primary eigenvector of the emission line correlation matrix of PG quasars studied by Boroson & Green (1992). This eigenvector 1 was later found to correlate with UV properties such as C IV shift/asymmetry (Marziani et al. 1996), Si III]/C III] ratio, and C IV and N V strength (Wills et al. 1999; Shang et al. 2003). Since eigenvector 1 was found to correlate significantly with X-ray properties (Laor et al. 1997; Brandt & Boller 1998), which are determined in the vicinity of the central black hole, it was suggested that differences in emission line properties revealed by eigenvector 1 are caused by differing central engine parameters (e.g., $L/L_{\rm Edd}$, accretion rate, orientation, and/or black hole spin). It was found that eigenvector 1 together with eigenvector 2 provide a parameter-space in which all major classes of broad-line sources can be discriminated, constituting a possible "H-R diagram" for quasars (Sulentic et al. 2000; Boroson 2002).

Another famous correlation involving quasar spectra is the anticorrelation between the equivalent width of the broad emission lines and the UV luminosity, called the Baldwin effect (Baldwin 1977). The appeal of this correlation was soon realized, since the luminosity of a distant quasar could

TABLE 1

List of Objects and Spectra

Designation (J2000) (1)	Name (2)	Type[a] (3)	Redshift (4)	N_H[b] (5)	Spectra (6)
0005+0203	Q0003+0146	Q	0.234	3.00	0005+0203oa
0006+2012	Mrk 335	Sy 1.2	0.026	3.70	0006+2012oa
0018+1629	QSO 0015+162	Q	0.553	4.00	0018+1629oa
0020+0226	Q0017+0209	Q	0.401	3.10	0020+0226oa
0020+2842	QSO 0020+287	Q	0.513	4.30	0020+2842oa
0029+1316	PG 0026+129	Q/Sy 1	0.142	4.90	0029+1316[oa–ob]
0039−5117	WPVS 007	NLS 1	0.029	2.40	0039−5117oa
0044−2434	Q0042−248	Q	0.807	1.50	0044−2434oa
0044+1026	MC 0042+101	Q	0.583	5.20	0044+1026oa
0048+3157	Mrk 348	Sy 2	0.015	5.90	0048+3157oa
0053+1241	I ZW 1	NLS 1	0.061	5.00	0053+1241oa
0103+0221	UM 301	Q	0.393	2.40	0103+0221oa
0104−2657	CT 336	Q	0.780	1.90	0104−2657oa
0109−1521	QSO 0107−156	Q	0.861	1.70	0109−1521oa
0110−0216	Q0107−0232	Q	0.728	8.00	0110−0216oa
0110−0219	Q0107−025A	Q	0.960	4.00	0110−0219oA
	Q0107−025B	Q	0.960	4.00	0110−0219oB
0120+2133	PG 0117+213	Q	1.493	4.80	0120+2133[oa–ob]
0122−0421	PKS 0119−04	Q	1.925	4.20	0122−0421oa
0124+0343	NGC 520.48	Q	0.336	2.00	0124+0343oa
0139+0131	PHL 1093	Q	0.260	3.10	0139+0131oa
0143+0220	Mrk 573	Sy 2	0.017	2.60	0143+0220oa
0201−1132	3C 57	Q	0.669	1.80	0201−1132oa
0206−0017	Mrk 1018	Sy 1.5	0.042	2.50	0206−0017oa
0217+1104	PKS 0214+10	Sy 1	0.408	6.40	0217+1104oa
0235−0402	PKS 0232−04	Q	1.450	2.20	0235−0402oa
0238+1636*	AO 0235+164	BL Lac	0.940	7.60	0238+1636ob
0241−0815	NGC 1052	Sy 2	0.005	2.90	0241−0815[oa–ob]
0251+4315	S4 0248+43	Q	1.310	10.10	0251+4315oa
0256−3315	PKS 0254−33	Q	1.915	2.30	0256−3315[oa–ob]
0304−2211	1E 0302−223	Q	1.400	1.80	0304−2211oa
0320−1926	0318−196	Q	0.104	2.80	0320−1926oa
0336+3218	NRAO 140	Q	1.258	14.20	0336+3218oa
0347+0105	IRAS 0345+0055	Q	0.031	8.80	0347+0105oa
0351−2744	PKS 0349−27	NLRG	0.066	0.90	0351−2744oa
0357−4812	PKS 0355−48	Q	1.005	1.10	0357−4812[oa–ob]
0417−0553	PKS 0414−06	Q	0.775	4.30	0417−0553oa
0423−0120	PKS 0420−01	Q	0.915	9.40	0423−0120oa
0424+0204	PKS 0421+01	Q	2.044	10.50	0424+0204oa
0452−2953	IRAS 0450−2958	Q	0.286	1.30	0452−2953oa
0456+0400	PKS 0454+039	Q	1.345	6.60	0456+0400oa
0516−0008	AKN 120	Sy 1	0.033	10.30	0516−0008oa
0519−4546	PKS 0518−45	Sy 1	0.035	4.10	0519−4546oa
0552−0727	NGC 2110	Sy 2/LINER	0.008	18.60	0552−0727oa
0630+6905	HS 0624+6907	Q	0.370	6.30	0630+6905oa
0741+3111	OI 363	Q	0.635	4.90	0741+3111oa
0742+6510	Mrk 78	Sy 2	0.037	4.00	0742+6510[oa–oj]
0743−6726	PKS 0743−67	Q	1.510	11.90	0743−6726oa
0804+0506	Mrk 1210	Sy 2	0.014	3.40	0804+0506oa
0813+4813	3C 196.0	Q	0.871	4.90	0813+4813oa
0830+2410	B2 0827+24	Q	0.939	3.00	0830+2410[0a–ob]
0838+2453	NGC 2622	Sy 1.8	0.029	3.30	0838+2453oa
0851+1612	Q0848+163	Q	1.936	2.40	0851+1612oa
0853+5118	NGC 2681	Q	0.002	2.50	0853+5118oa
0909−0932	QSO 0909−095	Q	0.646	4.50	0909−0932oa
0948+4039	4C 40.24	Q	1.252	1.30	0948+4039oa
0950+3926	PG 0947+396	Sy 1	0.206	1.90	0950+3926oa
0955+6903	NGC 3031	Sy 1.8	0.000	4.30	0955+6903[oa–oc]
1001+5553	0957+561A	Q	1.414	0.70	1001+5553oA
	0957+561B	Q	1.414	0.70	1001+5553oB
1004+0513	PG 1001+054	Q	0.161	1.80	1004+0513oa
1004+2225	PKS 1001+22	Q	0.974	3.10	1004+2225oa
1017−2046	J03.13A	Q	2.545	6.00	1017−2046oA
	J03.13B	Q	2.545	6.00	1017−2046oB

TABLE 1—*Continued*

Designation (J2000) (1)	Name (2)	Type[a] (3)	Redshift (4)	N_H[b] (5)	Spectra (6)
1019+2744	TON 34	Q	1.928	2.60	1019+2744oa
1028−0100	Q1026−0045−A	Q	1.437	4.80	1028−0100oA
	Q1026−0045−B	Q	1.437	4.80	1028−0100oB
1030+3102	B2 1028+313	Q	0.178	0.50	1030+3102oa
1034+3938	ZW 212.025	Sy 1	0.042	1.40	1034+3938oa
1041+0610	4C 06.41	Q	1.270	2.80	1041+0610oa
1048−2509	NGC 3393	Sy 2	0.012	5.80	1048−2509oa
1052+6125	4C 61.20	Q	0.422	0.90	1052+6125oa
1058+1951	PKS 1055+20	Q	1.110	1.80	1058+1951oa
1101+1102	Mrk 728	Sy 1.9	0.036	2.10	1101+1102oa
1106+7234	NGC 3516	Sy 1.5	0.009	2.90	1106+7234[oa−oe]
1117+4413	PG 1114+445	Q	0.144	1.90	1117+4413[oa−ob]
1118+0745	PG 1115+080A1	Q	1.718	3.50	1118+0745oA
	PG 1115+080A2	Q	1.718	3.50	1118+0745oB
1118+4025	PG 1115+407	Sy 1	0.154	1.70	1118+4025oa
1119+2119	PG 1116+215	Q	0.176	1.40	1119+2119oa
1121+1236	MC 1118+12	Q	0.685	2.30	1121+1236oa
1124+4201	Q1121+423	Q	0.234	2.30	1124+4201oa
1126+3515	Mrk 423	Sy 1.9	0.032	1.90	1126+3515oa
1127+2654	QSO 1127+269	Q	0.378	1.40	1127+2654oa
1130−1449	PKS 1127−14	Q	1.187	3.80	1130−1449oa
1135−0318	Q1132−0302	Q	0.237	3.50	1135−0318oa
1139+3154	NGC 3786	Sy 1.8	0.009	2.20	1139+3154oa
1141+0148	Q1138+0204	Q	0.383	2.30	1141+0148oa
1147−0132	Q1144−0115	Q	0.382	2.30	1147−0132oa
1148+1047	1146+111B	Q	1.010	3.60	1148+1047oB
1148+1050	1146+111C	Q	1.010	3.60	1148+1050oC
1148+1046	1146+111E	Q	1.100	3.60	1148+1046oE
1148+1054	MC 1146+111	Q	0.863	3.60	1148+1054oa
1151+5437	PG 1148+549	Q	0.969	0.90	1151+5437oa
1151+3825	B2 1148+387	Q	1.303	2.10	1151+3825oa
1153+4931	LB 2136	Q	0.334	2.10	1153+4931oa
1159+2106	TEX 1156+213	Q	0.349	2.20	1159+2106oa
1159+2914	4C 29.45	Q	0.729	1.50	1159+2914oa
1204+2754	GQ COMAE	Sy 1	0.165	1.70	1204+2754oa
1204+3110	UGC 7064	Sy 1.9	0.025	1.60	1204+3110oa
1210+3924	NGC 4151	Q	0.003	2.10	1210+3924oa
1216+1748	Q1214+1804	Q	0.374	2.70	1216+1748oa
1217+6407	4C 64.15	Q	1.288	2.30	1217+6407oa
1219+0545	QSO1219+057	Q	0.114	1.60	1219+0545oa
1221+0430	1219+047	Q	0.094	1.60	1221+0430[oa−ob]
1223+1545	1220+1601	Q	0.081	2.30	1223+1545[oa−ob]
1230+1223	NGC 4486	NLRG	0.004	2.50	1230+1223[ob−od]
1231−0224	PKS 1229−02	Q	1.045	2.30	1231−0224oa
1237+1149	NGC 4579	Sy 1.9	0.005	3.00	1237+1149oa
1239−1137	NGC 4594	Q	0.004	3.70	1239−1137oa
1240−3645	IC 3639	Sy 2	0.011	5.60	1240−3645oa
1250+2631	PG 1247+267	Q	2.038	0.80	1250+2631[oa−ob]
1250+3016	B2 1248+30	Q	1.061	1.10	1250+3016oa
1250+3125	CSO 173	Q	1.020	1.20	1250+3125oa
1250+3951	PG 1248+401	Q	1.030	1.30	1250+3951oa
1252+2913	CSO 176	Q	0.820	1.10	1252+2913oa
1253+3105	CSO 179	Q	0.780	1.20	1253+3105oa
1256−0547	3C 279	Q	0.536	2.20	1256−0547oa
1256+5652	Mrk 231	Sy 1	0.042	1.00	1256+5652oa
1301+2819	Q1258+285	Q	1.360	3.00	1301+2819oa
1305−1033	PKS 1302−102	Q	0.278	3.20	1305−1033oa
1307+0642	3C 281	Q	0.602	2.20	1307+0642oa
1310+4601	HS 1307+4617	Q	2.080	1.20	1310+4601oa
1312+3515	PG 1309+355	Sy 1.2	0.184	1.00	1312+3515oa
1314+0201	Q1311+0217	Q	0.306	2.00	1314+0201oa
1321+2847	TON 156	Q	0.549	1.20	1321+2847oa
1323+2910	TON 157	Q	0.960	1.10	1323+2910oa
1323+6541	PG 1322+659	Q	0.168	1.80	1323+6541[oa−ob]
1324+0537	IRAS 1321+0552	Q	0.205	2.30	1324+0537oa
1325+6515	4C 65.15	Q	1.618	1.90	1325+6515oa

TABLE 1—*Continued*

Designation (J2000) (1)	Name (2)	Type[a] (3)	Redshift (4)	N_H[b] (5)	Spectra (6)
1331+3030	3C 286.0	Q	0.849	1.10	1331+3030oa
1331+4101	PG 1329+412	Q	1.930	0.70	1331+4101oa
1337+2423	IRAS13349+2438	Sy 1	0.108	1.00	1337+2423[oa–ob]
1338+0432	NGC 5252	Sy 1.9	0.023	2.00	1338+0432[oa–ob]
1341+6740	Mrk 270	Sy 2	0.009	1.80	1341+6740oa
1342−0053	Q1340−0038	Q	0.326	2.10	1342−0053oa
1348+2622	QSO 1348+263	Q	0.597	1.10	1348+2622oa
1354+3139	B2 1351+31	Q	1.326	1.20	1354+3139oa
1354+1805	PG 1352+183	Q	0.152	1.80	1354+1805oa
1354+0052	PG 1352+011	Q	1.117	2.00	1354+0052oa
1405+2555	PG 1402+261	Sy 1	0.164	1.40	1405+2555[oa–ob]
1406+2223	PG 1404+226	Sy 1	0.098	2.00	1406+2223oa
1417+4456	PG 1415+451	Q	0.114	0.90	1417+4456oa
1419−1310	PG 1416−129	Q	0.129	7.20	1419−1310oa
1419+0628	3C 298	Q	1.436	2.00	1419+0628oa
1424+2256	QSO 1422+231A	Q	3.620	2.50	1424+2256oA
	QSO 1422+231B	Q	3.620	2.50	1424+2256oB
	QSO 1422+231C	Q	3.620	2.50	1424+2256oC
	QSO 1422+231D	Q	3.620	2.50	1424+2256oD
1427+2632	B2 1425+267	Q	0.366	1.50	1427+2632oa
1429+4747	PG 1427+480	Q	0.221	1.60	1429+4747oa
1432−4410	NGC 5643	Sy 2	0.004	8.50	1432−4410oa
1437−0147	Q1435−0134	Q	1.310	3.60	1437−0147[oa–ob]
1442+3526	Mrk 478	NLS 1	0.079	0.90	1442+3526[oa–ob]
1442−1715	NGC 5728	Sy 2	0.009	7.60	1442−1715oa
1446+4035	PG 1444+407	Sy 1	0.267	1.00	1446+4035oa
1454−3747	PKS 1451−375	Q	0.314	6.20	1454−3747oa
1504+6856	B2 1503+691	Q	0.318	2.20	1504+6856oa
1519+2346	LB 9612	Q	1.898	3.90	1519+2346oa
1519+2347	LB 9605	Q	1.834	3.90	1519+2347oa
1524+0958	PG 1522+101	Q	1.321	2.60	1524+0958oa
1526+4140	NGC 5929	Sy 2	0.008	1.90	1526+4140oa
1545+4846	1543+489	Q	0.400	1.60	1545+4846oa
1559+3501	Mrk 493	Sy 1	0.032	2.00	1559+3501oa
1617+3222	3C 332	Sy 1?	0.152	2.00	1617+3222oa
1624+2345	3C 336.0	Q	0.927	4.50	1624+2345oa
1627+5522	PG 1626+554	Sy 1	0.133	1.50	1627+5522oa
1629+2426	Mrk 883	Sy 1.9	0.038	3.80	1629+2426oa
1632+3737	PG 1630+377	Q	1.466	0.90	1632+3737oa
1642+3948	3C 345	Q	0.593	0.80	1642+3948oa
1658+0515	PKS 1656+053	Q	0.879	6.10	1658+0515oa
1716+5328	PG 1715+535	Q	1.920	2.40	1716+5328oa
1719+4858	ARP 102B	LINER	0.024	2.20	1719+4858oa
1719+4804	PG 1718+481	Q	1.084	2.10	1719+4804oa
1755+1820	NGC 6500	LINER	0.010	6.90	1755+1820oa
1800+7828	S5 1803+78	Q	0.680	3.60	1800+7828oa
1842+7946	3C 390.3	Sy 1	0.056	3.60	1842+7946oa
1902+3159	3C 395	Sy 1.5	0.635	11.00	1902+3159oa
1927+7358	4C 73.18	Q	0.302	7.20	1927+7358oa
1959+4044	Cygnus A	Q	0.056	33.00	1959+4044oa
2118+2626	NGC 7052	Q	0.014	9.60	2118+2626oa
2156+0722	Mrk 516	Sy 1.8	0.028	4.50	2156+0722oa
2242+2943	AKN 564	Sy 1.8	0.024	6.20	2242+2943oa
2253+1608	3C 454.3	Q	0.859	6.90	2253+1608oa
2254−1734	MR 2251−178	Sy 1	0.068	2.70	2254−1734oa
2303+0852	NGC 7469	Sy 1.2	0.016	4.80	2303+0852oa
2304+0311	PG 2302+029	Q	1.044	4.90	2304+0311oa

NOTE.—Table 1 is also available in machine-readable form in the electronic edition of the *Astrophysical Journal Supplement*.
[a] AGN type: (Q) QSO, (Sy) Seyfert, (NLS 1) narrow-line Seyfert 1, and (NLRG) narrow-line radio galaxy.
[b] N_H is in units of 10^{20} cm^{-2}. (*) We include this BL Lac object as it shows weak emission lines.

potentially be estimated from the emission line equivalent widths, providing a standard candle in measuring cosmological distances. In reality, the scatter of the Baldwin effect is too large to give meaningful results, and studies have concentrated on understanding and reducing this scatter (Shang et al. 2003; Dietrich et al. 2002). Conflicting results have also emerged, where radio-loud samples and samples with a wide range of luminosities show a stronger effect (e.g., Baldwin et al. 1978; Wampler et al. 1984; Kinney, Rivolo, & Koratkar 1990; Wang, Lu, & Zhou 1998), while radio-quiet samples and samples with a small luminosity range show weaker or no effect (e.g., Steidel & Sargent 1991; Wilkes et al. 1999). A number of explanations have been introduced to explain the Baldwin effect. It can be either due to geometry as in Netzer, Laor, & Gondhalekar (1992), where the inclination of the disk changes the apparent luminosity, or due to changes in spectral energy distribution with luminosity, where more luminous objects have softer ionizing continuum (Zheng & Malkan 1993; Green 1998) or due to a decrease of covering factor of the broad emission line clouds with luminosity (Wu, Boggess, & Gull 1983). There have also been claims that the Baldwin effect is affected by evolution (Green, Forster, & Kuraszkiewicz 2001) or may be due to selection effects (continuum beaming, biases in selection techniques—see Sulentic et al. 2000; Yuan, Siebert, & Brinkmann 1998).

Despite a vigorous study of emission line properties of AGNs in the last 30 years, which resulted in few thousand published articles, questions about the structure and kinematics of the BLR and their relationship to the central engine (accretion mechanism, origin of the fuel, etc.) have not been answered. Nor is it clear how the BLR relates to the other components seen in AGN spectra: broad and narrow absorption lines, X-ray warm absorbers, high-ionization emission lines, and scattering regions. Despite attempts to unite these components (Elvis 2000; Laor & Brandt 2002; Ganguly et al. 2001; Murray & Chiang 1995) definitive tests have been elusive. Progress has been hampered by lack of large data sets with uniform and reliable measurements of emission lines that would consistently measure the continuum and account for blended iron emission, which heavily contaminates emission lines such as Hβ, Mg II, and C III] and forms a pseudocontinuum complicating the measurements of the broadband continuum, the weaker lines, and the wings of strong emission lines (Wills, Netzer, & Wills 1985; Boroson & Green 1992; Vestergaard & Wilkes 2001). Most studies have concentrated either on large nonuniform samples where emission line measurements have been compiled from literature (Zheng & Malkan 1993; Zamorani et al. 1992; Corbin & Boroson 1996; Dietrich et al. 2002) or small samples with uniform measurements (Boroson & Green 1992; Wills et al. 1999; Wilkes et al. 1999).

We have therefore undertaken a major study of AGN emission lines, where our largely automated procedure accounts for Galactic extinction, models blended optical and UV iron emission, includes Galactic and intrinsic absorption lines, and models emission lines using multiple Gaussians. Using the same modeling procedure we have previously analyzed and published measurements of emission lines of two large data sets. The first 993 spectra from the Large Bright Quasar Survey has been presented by Forster et al. (2001, hereafter Paper I) together with detailed description of our analysis methods. The second includes 174 *Hubble Space Telescope* Faint Object Spectrograph (*HST* FOS) spectra obtained before the installation of COSTAR and was presented in Kuraszkiewicz et al. (2002, hereafter Paper II). In the current paper we present the measurements of emission lines and plots of spectral fits of the remaining 220 *HST* FOS spectra that were observed after the installation of COSTAR, completing the analysis of all archival *HST* FOS spectra. Statistical comparison of the emission-line parameters and continuum parameters of these large samples will hopefully bring us closer to building an accurate model of emission line regions and their dependence on the central engine.

2. THE POST-COSTAR FOS ACTIVE GALACTIC NUCLEUS SAMPLE

The sample was assembled by cross-correlating the Veron-Cetty & Veron (1996) catalog of AGNs with the MAST (Multimission Archive at Space Telescope) holdings. BL Lac objects were ignored, as their spectra show no emission lines. Starburst galaxies and broad absorption line (BAL) quasars (where emission lines are heavily disrupted by absorption features) were not included. We chose all available (UV and optical) spectrophotometric archival data that have been observed with the Faint Object Spectrograph (FOS; Keyes et al. 1995 and references therein) on *HST* after the installation of COSTAR (i.e., after 1993 December). FOS spectra obtained prior to 1993 December have been analyzed by us in Paper II. We include all spectra taken with the high-resolution gratings (G130H, G190H, G270H, G400H, G570H, G780H; spectral resolution $\lambda/\Delta\lambda \sim 1300$). Low-resolution (G160L, G650L; spectral resolution $\lambda/\Delta\lambda \sim 250$) gratings were also included when high-resolution gratings were not available in the matching wavelength range. Spectra obtained with the prism were excluded as their extremely low resolution precludes any reasonable emission line measurements. We analyzed only spectra with a mean signal-to-noise (S/N) per resolution element $\geq$5.

The FOS spectra were uniformly calibrated to account for temporal, wavelength- and aperture-dependent variations that are seen in the instrumental response. We use the most recent version of the FOS calibration pipeline with the ST-ECF POA version of *calfos*. This pipeline provides an improved correction to the zero point offsets in the BLUE high-resolution spectra, removes hot pixel/hot diode regions from individual exposures, and calibrates spectra to the 4.″3 aperture.

We interpolated all of the spectra to a linear wavelength scale, retaining the original approximate wavelength intervals (in Å per bin), and, for each object, we averaged all of the spectra obtained at a particular wavelength setting if the flux did not differ by more than 20%. If the difference in flux was larger, the spectra were analyzed separately. To obtain a reliable continuum fit for each object, we combined spectra obtained at different wavelength settings and observed at different times if the flux levels did not differ by more than 20% in the overlap region. High-resolution gratings (G130H, G190H, G270H, G400H, G570H, G780H) were merged separately from the low-resolution gratings (G160L, G650L). In both cases, the longer wavelength spectrum was scaled to match the shorter wavelength spectrum and the spectra were then spliced at wavelengths in continuum regions away from emission or absorption lines by retaining as much of the higher S/N spectrum as possible.

At this point the sample consisted of 327 spectra. Spectra that showed no emission lines, due to a too low S/N ($<$5) in the line regions, or a redshift that placed strong emission lines outside the spectrum's wavelength range (mostly chosen for studies of

TABLE 2
REPRESENTATIVE LIST OF OBJECTS AND FOS SPECTRA

Spectrum	Data Set	Configuration	Grating	Exposure Time (s)	Time of Observation
0005+0203oa.....	Y29C0102T	RD	G190H	1379.9	1994 Jul 21
0006+2012oa.....	Y29E0202T	BL	G130H	1389.9	1994 Dec 16
	Y29E0203T	BL	G130H	769.9	1994 Dec 16
	Y29E0204T	BL	G190H	960.0	1994 Dec 16
	Y29E0205T	BL	G270H	60.0	1994 Dec 16
	Y29E0206T	BL	G270H	420.0	1994 Dec 16
0018+1629oa.....	Y3IS0105T	RD	G190H	1080.0	1997 Jan 30
	Y3IS0106T	RD	G190H	2409.9	1997 Jan 30
	Y3IS0107T	RD	G190H	2409.9	1997 Jan 30
	Y3IS0108T	RD	G190H	2409.9	1997 Jan 30
	Y3IS0109T	RD	G190H	2409.9	1997 Jan 30
	Y3IS010AT	RD	G190H	2409.9	1997 Jan 30
	Y3IS010BT	RD	G190H	1519.9	1997 Jan 30
0020+0226oa.....	Y29C0202T	RD	G190H	1369.9	1994 Aug 06
	Y29C0203T	RD	G190H	423.9	1994 Aug 06
0020+2842oa.....	Y3AG0102T	RD	G270H	1479.9	1996 Nov 17
	Y3AG0103T	RD	G270H	2430.0	1996 Nov 17
	Y3AG0104T	RD	G270H	2430.0	1996 Nov 17
	Y3AG0105T	RD	G270H	2430.0	1996 Nov 17
0029+1316oa.....	Y27O0302T	BL	G130H	720.0	1994 Jul 30
0029+1316ob	Y2JK0102T	BL	G130H	1469.9	1994 Nov 27
	Y2JK0103T	BL	G130H	2149.9	1994 Nov 27
	Y2JK0104T	BL	G130H	2149.9	1994 Nov 27
	Y2JK0105T	BL	G130H	2149.9	1994 Nov 27
	Y2JK0106T	BL	G130H	1680.0	1994 Nov 27
	Y2JK0108T	RD	G270H	539.9	1994 Nov 27
	Y2JK0109T	RD	G190H	827.9	1994 Nov 27

NOTE.—Table 2 is available in its entirety in the electronic edition of the *Astrophysical Journal Supplement*. A portion is shown here for guidance regarding its form and content.

the Lyα forest), were then removed. The final sample consists of 220 spectra of the 180 AGNs listed in Table 1. In the first column the coordinate designation based on the equinox J2000 position is given, followed by the AGN name (col. [2]), AGN type and redshift (from the NASA/IPAC Extragalactic Database), and Galactic $N_{\rm H}$ in units of 10^{20} cm^{-2} (cols. [3]–[5]). The values of $N_{\rm H}$ are in general taken from the Bell Laboratory H I survey (Stark et al. 1992). In a few cases for which $N_{\rm H}$ had been specifically measured, we quote the values from the literature (Lockman & Savage 1995; Elvis, Wilkes, & Lockman 1989); for objects with declination greater than 40°, $N_{\rm H}$ is from Heiles & Cleary (1979). The last column of Table 1 gives the list of spectra that were analyzed for each object. The name of the spectrum consists of the coordinate designation from column (1), followed by a two letter designation: "o" indicates a post-COSTAR spectrum (in Paper II pre-COSTAR spectra were designated with "r"); a second letter (a to z) indicates whether the AGN in question has more than one spectrum available. A capital letter indicates a spectrum of a lensed component as e.g., in 1001+5553oA and 1001+5553oB. In Table 2 we show a detailed list of FOS gratings, and data sets with exposure times that were used to compile spectra listed in Table 1.

3. ANALYSIS OF SPECTRA

3.1. *Continuum and Blended Iron Fitting*

Since our goal was to assemble a uniform database of emission line measurements, we have analyzed our post-COSTAR spectra following the same fitting procedures as those used in the LBQS and pre-COSTAR/FOS spectral analysis (for details see Papers I and II). We used the modeling software *Sherpa*[1] (Freeman, Doe, & Siemiginowska 2001) developed for the *Chandra* mission, where the model parameters were determined from a minimization of the χ^2 statistic with modified calculation of uncertainties in each bin (Gehrels 1986) and using the Powell optimization method for continuum, iron emission, and first emission line fits and the Levenberg-Marquardt optimization method in the final emission line fits (see below). First, we fitted a reddened power-law continuum[2] to regions of the spectrum redward of Lyα and away from strong emission lines and blended iron emission. We use the same continuum windows as in the analysis of pre-COSTAR continuum spectra (see Table 2 in Paper II), with the addition of a new window redward of Hα at 6990–7020 Å rest frame. Most of the post-COSTAR spectra were fitted by a single power law. However, in 21 spectra that covered a large wavelength range, two power laws were introduced: one (UV) extending at $\lambda_{\rm rest} < 4200$ Å and another (optical) at $\lambda_{\rm rest} > 4200$ Å, both normalized at $\lambda = 4200$ Å. In Table 3 we present the slopes of the dereddened UV and optical continua (cols. [2] and [5], respectively) with the normalization of the continuum in units of 10^{-14} ergs cm^{-2} s^{-1} Å^{-1} (col. [3]) at the observed wavelength $\lambda_{\rm norm}$ (col. [4]). The slopes and normalizations are quoted with 2 σ errors. For spectra with only one continuum window present, a constant slope of $\Gamma = 1$ is quoted

[1] http://cxc.harvard.edu/sherpa/index.html.
[2] We use the reddening curves of Cardelli et al. 1989 to account for Galactic extinction; see Paper I for details.

TABLE 3
CONTINUUM PARAMETERS

Designation (1)	Γ_{UV}[a] (2)	Norm.[b] (3)	λ_{norm} (4)	Γ_{opt}[a] (5)
0005+0203oa.....	$0.17^{+0.19}_{-0.23}$	$0.382^{+0.009}_{-0.009}$	1804.7	...
0006+2012oa.....	$1.46^{+0.02}_{-0.01}$	$9.579^{+0.057}_{-0.068}$	1499.9	...
0018+1629oa.....	$1.92^{+0.25}_{-0.24}$	$0.058^{+0.001}_{-0.001}$	2271.3	...
0020+0226oa.....	$-0.77^{+0.79}_{-0.86}$	$0.194^{+0.006}_{-0.006}$	2049.0	...
0020+2842oa.....	$2.08^{+0.12}_{-0.10}$	$0.049^{+0.001}_{-0.001}$	2227.3	...
0029+1316oa.....	1	$2.905^{+0.189}_{-0.189}$	1513.1	...
0029+1316ob	$1.14^{+0.03}_{-0.02}$	$2.028^{+0.016}_{-0.018}$	1670.2	...
0039−5117oa*.....	$0.28^{+0.04}_{-0.04}$	$0.336^{+0.019}_{-0.001}$	3000.0	$2.00^{+0.05}_{-0.02}$
0044+1026oa.....	$0.31^{+0.51}_{-0.48}$	$0.036^{+0.002}_{-0.002}$	2315.1	...
0044−2434oa.....	$0.91^{+0.83}_{-0.05}$	$0.079^{+0.006}_{-0.000}$	2642.7	...
0048+3157oa.....	$0.94^{+0.55}_{-0.88}$	$0.019^{+0.006}_{-0.003}$	2271.3	...
0053+1241oa.....	$0.89^{+0.01}_{-0.01}$	$2.881^{+0.009}_{-0.011}$	1798.6	...
0103+0221oa.....	$1.37^{+0.44}_{-0.46}$	$0.267^{+0.007}_{-0.007}$	2037.3	...
0104−2657oa.....	1	$0.164^{+0.002}_{-0.002}$	2273.9	...
0109−1521oa.....	$1.44^{+0.12}_{-0.12}$	$0.070^{+0.001}_{-0.001}$	2721.7	...
0110−0216oa.....	1	$0.078^{+0.001}_{-0.001}$	2289.6	...
0110−0219oA.....	$2.01^{+0.08}_{-0.32}$	$0.100^{+0.000}_{-0.002}$	2866.5	...
0110−0219oB.....	$1.86^{+0.13}_{-0.13}$	$0.205^{+0.002}_{-0.002}$	2866.5	...
0120+2133oa.....	1	$0.565^{+0.011}_{-0.011}$	3184.8	...
0120+2133ob	1	$0.227^{+0.020}_{-0.020}$	3289.1	...
0122−0421oa.....	1	$0.086^{+0.003}_{-0.003}$	3272.2	...
0124+0343oa.....	$0.48^{+0.06}_{-0.05}$	$0.021^{+0.000}_{-0.000}$	2264.5	...
0139+0131oa.....	$1.03^{+0.12}_{-0.10}$	$0.084^{+0.003}_{-0.003}$	1842.8	...

NOTES.— Table 3 is published in its entirety in the electronic edition of the *Astrophysical Journal Supplement*. A portion is shown here for guidance regarding its form and content. (*) See Appendix for notes on individual spectra.

[a] The power-law continuum slopes Γ_{UV} and Γ_{opt} are defined as $f_\lambda \propto \lambda^{-\Gamma}$. Γ_{UV} is fitted at $\lambda_{rest} < 4200$, Γ_{opt} at $\lambda_{rest} > 4200$. Slopes with no listed errors show the assumed slope value in cases where only a single continuum window was available.

[b] Normalization of the UV power law in units of 10^{-14} ergs cm^{-2} s^{-1} Å^{-1}, at observed wavelength λ_{norm}.

without errors. This value was adopted since the mean slope of the pre- and post-COSTAR FOS sample is 0.97 ± 0.09.

The next step in our fitting procedure was to model the blended iron emission lines. In the UV we used the Vestergaard & Wilkes (2001) iron template covering rest-frame wavelengths between 1250 and 3100 Å, while in the optical we used the Boroson & Green (1992) template covering 4250–7000 Å. First, a crude estimate of the template's flux normalization was obtained by fitting the 2000 km s^{-1} FWHM template to regions in which iron emission is known to be strongest (see col. [2] in Table 2 of Paper II). Then the FWHM of iron emission was estimated by comparing the spectrum with a grid of templates with FWHM between 900 and 10,000 km s^{-1} in steps of 250 km s^{-1}. This was followed by a fit of both the FWHM and flux normalization at the iron fitting windows, followed by two iterations of the continuum and iron fits (refer to Paper I for more details). At this point the continuum and iron fits results were inspected and adjustments were made to spectra not fitted successfully (5% of spectra needed adjustments of the continuum fit and three spectra needed adjustment of iron fits).

3.2. *Emission and Absorption Line Fitting*

The emission lines were generally fitted with one Gaussian. However, since most (95%) FOS spectra have high S/N, the strong emission lines (Lyα, C IV, C III], Mg II, Hβ, Hα) were fitted using two components: the very broad line region (VBLR) component and the intermediate line region (ILR; see Brotherton et al. 1994) here referred to as the broad and narrow components, respectively. We use exactly the same emission line inventory as in the pre-COSTAR spectra (see Table 3 in Paper II).

As a first stage, the FWHM and peak amplitude of the Gaussians are modeled while keeping the position of the emission line fixed at the expected wavelength (calculated from redshift). Then the position of the line is freed and modeled together with the FWHM and peak amplitude using Powell optimization. In the next step all Gaussian parameters are refitted, this time using distinct high and low *sigma rejection* criteria. We found that $\sigma = 3$ for low rejection omits most of the absorption lines superimposed on the emission lines, while $\sigma = 7$ for high rejection bypasses most spikes not associated with the emission line (e.g., geocoronal Lyα, cosmic rays, etc.). At this stage we use the Levenberg-Marquardt optimization method, which is faster than the Powell method but only works well if the statistical surface is well behaved (after two runs of the emission line parameter fitting with the Powell method, this was certainly the case). It is nearly impossible to design a fully automated procedure that can deal with the wide range of spectral shapes that AGNs show, so at this point the fits were inspected and adjustments were made to spectra where necessary. About 5% of spectra needed adjustments at least in one emission line fit.

For each spectrum, the continuum, iron, and emission line model obtained in the *Sherpa* fitting was next used as an input "continuum" to the FINDSL routine (Aldcroft 1993), which identifies narrow absorption lines and fits them with Gaussian

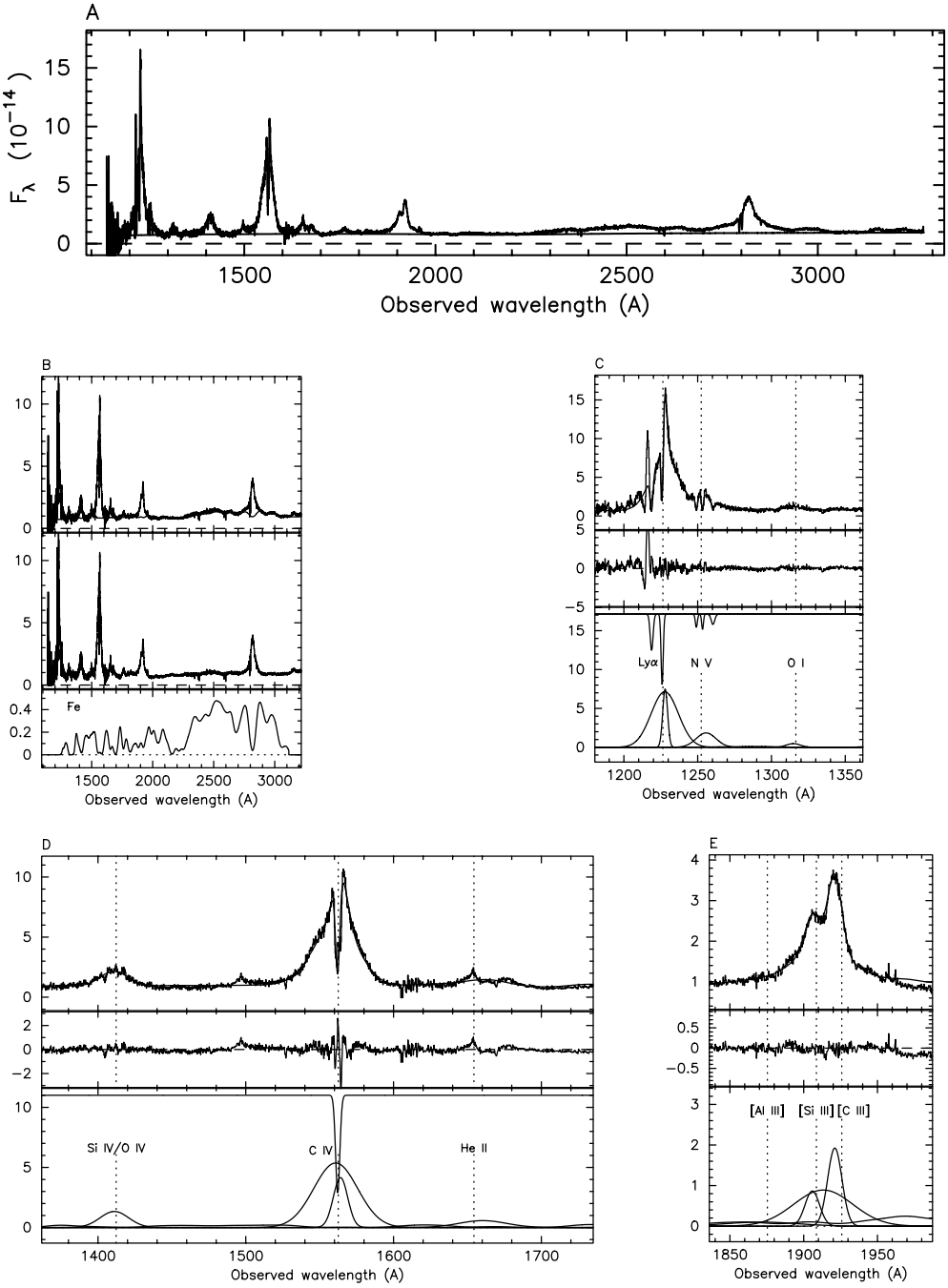

FIG. 1.—Example of spectral modeling of NGC 3516 (1106+7234oe, $z = 0.00880$, $N_{\rm H}$ Gal $= 2.90 \times 10^{20}$ cm^{-2}). Panel (*a*) shows the reddened power-law continuum model fitted redward of Lyα plotted over the observed spectrum. Below in (*b*) we show iron modeling, divided into three frames: (*top*) continuum+iron model plotted over the overall spectrum, (*middle*) iron-subtracted spectrum, and (*bottom*) fitted iron template. Panels (*c*), (*d*), and (*e*) show modeling of the Lyα, C IV, and C III] emission line regions, respectively. Each panel for each emission line region is divided into three frames: (*top*) total best-fit model plotted over the relevant region of each spectrum, (*middle*) residuals, and (*bottom*) individual Gaussian components. Strong emission lines such as Lyα, C IV, and C III] are modeled with two components—narrow and broad—while other emission lines are modeled using one Gaussian. The absorption lines that overlap each emission line are plotted at the top of the bottom frame. The dashed vertical lines in the emission line panels are drawn at the expected emission line position calculated using the redshift quoted at the top of the figure. Flux units are 10^{-14} ergs cm^{-2} s^{-1} Å^{-1}, and wavelength units are in Å and are observed frame values. [*See the electronic edition of the Journal for a color version of this figure.*]

profiles. We set the routine to find absorption lines away from the Lyα forest region (blueward of $\lambda_{\rm rest} = 1065$ Å) and outside the Balmer continuum region (3360–3960 Å), where the global power-law continuum may not fit the spectra well. The minimum significance level for identification of absorption lines was set to 4.5 σ (see Paper I for more details). We detect and fit absorption lines with $W_\lambda \geq 0.3$ Å. The absorption line parameters were then used in the next iterative modeling step where the position, peak amplitude, and FWHM of the absorption line were modeled simultaneously by the *Sherpa* program, followed by another iteration of the emission line fitting. After this stage the results were inspected and spectra refitted if the automated procedure did not perform well. An example of a full spectral fitting is shown in Figure 1. The top panel shows the reddened power-law continuum fit redward of Lyα to the observed spectrum, followed below by panels

showing blended iron and emission line modeling of Lyα, C IV, C III], and Mg II. Since the whole post-COSTAR FOS Spectral Atlas includes 220 spectra, we present similar plots of other spectral fits only on our Web site.[3]

3.3. *Error Analysis*

The error analysis follows the procedure from Paper I (see § 3.5 of that paper for details), in which the 2 σ errors for each emission line parameter were determined from the χ^2 confidence interval bounds ($\Delta\chi^2 = 4.0$) using the *uncertainty* procedure in *Sherpa*. The upper limits of equivalent widths were determined by fixing the line position at the expected wavelength, by fixing the FWHM at the value of the median FWHM found for that line in the LBQS sample (see col. [3], Table 3 of Paper II), and by setting the amplitude of the line to the 2 σ positive error.

4. EMISSION LINE MEASUREMENTS

In Table 4 we present the rest-frame emission line measurements for one example object NGC 3516 (spectrum 1106+7234oe). The format of Table 4 is exactly the same as the format of the electronic tables of emission line measurement presented for the LBQS and pre-COSTAR FOS samples, making it simple to analyze the LBQS and FOS samples together. In the full Table 4, each spectrum is represented by 43 rows, one for each possible emission line measurement. In the first column the name of the spectrum is given, followed by the object's redshift (col. [2]), followed by information on the emission line parameters: name of the emission line (col. [3]), FWHM in km s^{-1} (cols. [4]–[6] showing the value and $\pm$ 2 σ errors), the offset of the peak of the Gaussian emission line model (all lines except iron) in km s^{-1} from the expected position based on the tabulated redshift (cols. [7]–[9] value, $\pm$ 2 σ errors), the rest-frame equivalent width of the emission line in Å (cols. [10]–[12]) and the observed frame flux in units of 10^{-14} ergs cm^{-2} s^{-1} (cols. [13]–[15]). Errors quoted for flux and W_λ are based on the uncertainties in the amplitude and FWHM of the Gaussian model and do not include an error from an uncertainty in the underlying continuum flux level, which we estimate to be about 10%. For emission lines where only an upper limit on flux and W_λ is available, no values for the peak offset are quoted as the position of the line was fixed at the line's expected wavelength. Also, the FWHM value in this case was set to the median value for the LBQS sample (see Table 3 in Paper II) with no associated errors. Finally, the last column (16) in the full table gives the number of narrow absorption features used in the emission line modeling. Our Gaussian decomposition is not necessarily unique and may be sensitive to slight shifts in continuum placement. While the total flux and equivalent width are easily derived by summing values provided for individual Gaussian components, no simple combination yields a FWHM representative of the entire emission line. We therefore list in Table 4B the total line FWHM (with $\pm$2 σ errors) of those lines that have been modeled using two Gaussians. These are Lyα, C IV, C III], Mg II, Hβ, and Hα, where the width of the line was measured at half peak of the dereddened emission line model after excluding iron emission, absorption lines, and weaker emission lines (e.g., in the Lyα region we exclude the N V line, in the Hα region [N II] and [S II]).

5. STATISTICS AND COMPARISON WITH THE POST-COSTAR SAMPLE

The statistical properties of the rest-frame W_λ and FWHM distributions of the emission line measurements of the post-COSTAR spectra are presented in Table 5. The numbers quoted

[3] See http://hea-www.harvard.edu/ ~ pgreen/HRCULES.html.

TABLE 4
REPRESENTATIVE EMISSION LINE MEASUREMENTS

Emission Line (1)	FWHM (km s^{-1}) (2)	$\Delta v_{\rm peak}$ (km s^{-1}) (3)	W_λ (Å) (4)	Observed Flux (10^{-14} ergs cm^{-2} s^{-1}) (5)	Absorption Lines (6)
1106+7234oe, z = 0.00880					
UV iron	4250^{+5750}_{-250}	0^{+0}_{-0}	$164.40^{+2.10}_{-2.10}$	$195.90^{+2.50}_{-2.50}$	0
Optical iron	...	...	...	...	...
Lyβ	...	...	...	...	...
Lyα narrow.....	950^{+20}_{-80}	380^{+20}_{-20}	$41.60^{+1.80}_{-6.60}$	$49.70^{+2.10}_{-7.90}$	0
Lyα broad.....	5300^{+70}_{-70}	300^{+40}_{-40}	$225.40^{+6.20}_{-6.20}$	$269.50^{+7.40}_{-7.40}$	2
N V	3750^{+240}_{-90}	750^{+40}_{-140}	$41.30^{+4.80}_{-1.90}$	$49.40^{+5.70}_{-2.20}$	3
O I	2800^{+320}_{-280}	-350^{+200}_{-180}	$7.40^{+1.90}_{-1.60}$	$8.90^{+2.30}_{-1.90}$	0
Si IV + O IV].....	4850^{+140}_{-140}	-250^{+80}_{-80}	$40.20^{+2.40}_{-2.30}$	$48.10^{+2.90}_{-2.80}$	0
C IV narrow.....	2300^{+60}_{-60}	280^{+30}_{-30}	$63.60^{+3.30}_{-3.20}$	$76.20^{+4.00}_{-3.80}$	0
C IV broad	6700^{+50}_{-50}	-340^{+30}_{-30}	$240.80^{+4.10}_{-4.00}$	$288.40^{+4.90}_{-4.80}$	1
He II blend.....	6800^{+240}_{-300}	1050^{+180}_{-180}	$27.60^{+2.20}_{-2.40}$	$33.10^{+2.60}_{-2.90}$	0
Al III	9000^{+1700}_{-1500}	-800^{+800}_{-800}	$6.80^{+2.20}_{-1.80}$	$8.10^{+2.70}_{-2.10}$	0
Si III].....	1800^{+20}_{-900}	-440^{+40}_{-50}	$12.90^{+0.40}_{-7.30}$	$15.50^{+0.40}_{-8.70}$	0
C III] narrow.....	1800^{+10}_{-100}	-740^{+50}_{-10}	$28.30^{+0.40}_{-3.00}$	$33.90^{+0.50}_{-3.60}$	0
C III] broad.....	7400^{+40}_{-260}	-1950^{+50}_{-80}	$54.10^{+0.80}_{-4.00}$	$64.90^{+0.90}_{-4.80}$	0
Mg II narrow	2850^{+50}_{-50}	-620^{+30}_{-30}	$51.90^{+1.70}_{-1.70}$	$62.40^{+2.10}_{-2.10}$	0
Mg II broad	7550^{+30}_{-260}	-650^{+20}_{-100}	$103.40^{+1.10}_{-5.60}$	$124.40^{+1.30}_{-6.80}$	2

NOTES.—Table 4 is available in its entirety in the electronic edition of the *Astrophysical Journal Supplement*. A portion is shown here for guidance regarding its form and content. We present here line measurements for one, example spectrum 1106+7234oe. All measurements are rest frame except for flux. Spectral modeling of this object is shown in Fig. 1.

TABLE 5

REST-FRAME EMISSION LINE PARAMETER DISTRIBUTIONS

			W_λ (Å)					FWHM (km s^{-1})			
			Detected			Kaplan-Meier		Detected			
Emission Line (1)	Total (2)	Limits (3)	Mean (4)	SD (5)	Median (6)	Mean (7)	Median (8)	Num (9)	Mean (10)	SD (11)	Median (12)
UV iron	77	15	67 ± 11	87	54	54 ± 7	45	63	4537 ± 716	5683	3500
Optical iron	18	2	103 ± 42	169	18	91 ± 29	24	16	5809 ± 1860	7438	7200
Lyβ+O VI λ1035	77	4	22 ± 7	57	10	21 ± 6	10	73	7110 ± 1068	9129	5800
Lyα λ1216:											
Single[a]	13	0	710 ± 360	1299	145	...	...	13	4304 ± 1539	5549	4100
Narrow[b]	96	1	31 ± 5	51	19	39 ± 4	19	96	2526 ± 284	2787	2365
Broad	97	0	83 ± 13	126	64	...	...	96	10993 ± 1242	12167	11600
Sum[c,d]	108	0	153 ± 28	290	87	...	...	...	...	...	...
N V λ1241.5	108	8	12 ± 2	19	7	12 ± 1	6	98	4038 ± 481	4762	3475
O I λ1305	102	8	4 ± 1	6	2	3 ± 1	2	92	2722 ± 343	3294	2450
Si IV + O IV] λ1400	102	0	12 ± 2	17	9	...	...	102	5329 ± 594	5997	5400
C IV λ1549:											
Single[a]	4	0	42 ± 27	55	32	...	...	4	4525 ± 2683	5366	5100
Narrow	92	2	30 ± 5	45	22	30 ± 3	22	89	2670 ± 316	2979	2600
Broad	92	2	63 ± 10	90	43	62 ± 7	42	90	10281 ± 1203	11413	9910
Sum[c]	94	0	91 ± 13	125	67	...	...	...	...	...	...
He II λ1640	89	1	22 ± 3	27	18	22 ± 2	19	88	9037 ± 1071	10050	10000
Al III λ1859	68	5	7 ± 1	11	5	7 ± 1	4	62	4341 ± 673	5307	4600
Si III] λ1892	59	9	6 ± 2	17	2	6 ± 2	2	59	1306 ± 201	1547	1350
C III] λ1909:											
Single[a]	...	...	...	...	...	...	...	...	...	...	...
Narrow	68	2	13 ± 3	28	5	12 ± 3	5	66	1614 ± 222	1807	1575
Broad[e]	68	2	27 ± 5	36	20	26 ± 3	20	66	6547 ± 965	7840	5825
Sum[c,f]	66	0	35 ± 6	48	27	...	...	...	...	...	...
Mg II λ2800:											
Single[a]	4	0	104 ± 76	152	90	...	...	4	2887 ± 1846	3692	2525
Narrow	44	0	37 ± 13	86	17	...	...	42	2050 ± 347	2252	2050
Broad	44	0	47 ± 11	70	27	...	...	44	6751 ± 1136	7535	6550
Sum[c]	47	0	86 ± 21	143	50	...	...	...	...	...	...
[Ne V] λ3426	21	1	14 ± 7	32	3	13 ± 6	3	18	940 ± 306	1298	700
[O II] λ3728	21	0	138 ± 102	469	4	...	...	20	1008 ± 343	1534	570
[Ne III] λ3869	21	0	33 ± 19	87	6	...	...	21	1318 ± 440	2017	800
Hδ λ4101.7	17	2	42 ± 22	85	6	37 ± 16	4	14	2654 ± 1177	4404	1350
[S II] λ4072.5	17	10	38 ± 9	23	27	16 ± 10	1	7	717 ± 384	1017	600
Hγ λ4340.5	15	1	21 ± 10	37	11	20 ± 7	10	14	1309 ± 405	1514	1325
[O III] λ4363	15	3	13 ± 8	27	6	11 ± 5	1	12	663 ± 240	831	500
He II λ4686	17	2	10 ± 5	18	3	9 ± 3	2	15	2681 ± 1230	4764	1000
Hβ λ4861:											
Single[a]	5	0	31 ± 22	48	13	...	...	5	3220 ± 2190	4897	2100
Narrow	12	0	29 ± 12	42	20	...	...	12	1132 ± 411	1423	1010
Broad	12	0	90 ± 37	129	50	...	...	12	9090 ± 3491	12094	5150
Sum[c]	17	0	94 ± 34	141	59	...	...	...	...	...	...
[O III] λ4959	17	1	35 ± 17	69	10	33 ± 13	7	16	1045 ± 325	1300	890

TABLE 5—*Continued*

Emission Line (1)	Total (2)	Limits (3)	W_λ (Å) Detected Mean (4)	SD (5)	Median (6)	Kaplan-Meier Mean (7)	Median (8)	FWHM (km s^{-1}) Detected Num (9)	Mean (10)	SD (11)	Median (12)
UV iron											
[O III] λ5007	16	0	105 ± 52	209	31	...	...	16	1021 ± 297	1190	1015
He I λ5875.6	18	2	15 ± 5	18	13	13 ± 2	11	16	2254 ± 684	2737	2400
[N II] λ6548	26	1	25 ± 7	37	13	24 ± 5	7	24	615 ± 161	786	330
Hα λ6563:											
Single[a]	...	...	...	...	...	...	...	...	...	...	...
Narrow	26	0	120 ± 34	172	82	...	...	26	1362 ± 335	1708	950
Broad	26	0	190 ± 53	265	157	183 ± 35	145	25	4918 ± 1289	6446	3400
Sum[c]	26	0	203 ± 79	404	242	...	...	...	...	...	...
[N II] λ6583	26	2	43 ± 14	69	28	40 ± 10	23	24	518 ± 131	642	350
[S II] λ6716.4	21	1	17 ± 5	23	14	16 ± 3	13	20	603 ± 193	864	475
[S II] λ6731	20	1	16 ± 6	26	8	15 ± 4	7	20	376 ± 98	438	350

Notes.—Col. (1), emission line or line blend; col. (2), total number of emission lines modeled; col. (3), number of upper limits; col. (4), mean W_λ of detected emission lines; col. (5), standard deviation (SD) of W_λ measurements for detected emission lines; col. (6), median of W_λ for detections; cols. (7)–(8), Kaplan-Meier reconstructed mean and median of W_λ distribution when upper limits are present. Cols. (9)–(12), the number, mean, and median of the distribution of FWHM of the Gaussian components used to model each emission feature.

[a] The distribution for single Gaussian component models are tabulated separately from narrow and broad components.

[b] Means, medians, and SD of W_λ calculated excluding objects with high equivalent width measurements (PKS 0518−45 and NGC 3031).

[c] The distribution of the sum of the broad and narrow component W_λ measurements included with the single component measurements.

[d] Means, medians, and SD of W_λ calculated excluding objects with high equivalent width measurements (NGC 5728 and NGC 5643).

[e] Means, medians, and SD of W_λ calculated excluding objects with high equivalent width measurements (NGC 5252, NGC 4579, and NGC 5929).

[f] Means, medians, and SD of W_λ calculated excluding objects with high equivalent width measurements (NGC 5252, NGC 4579, and NGC 5728).

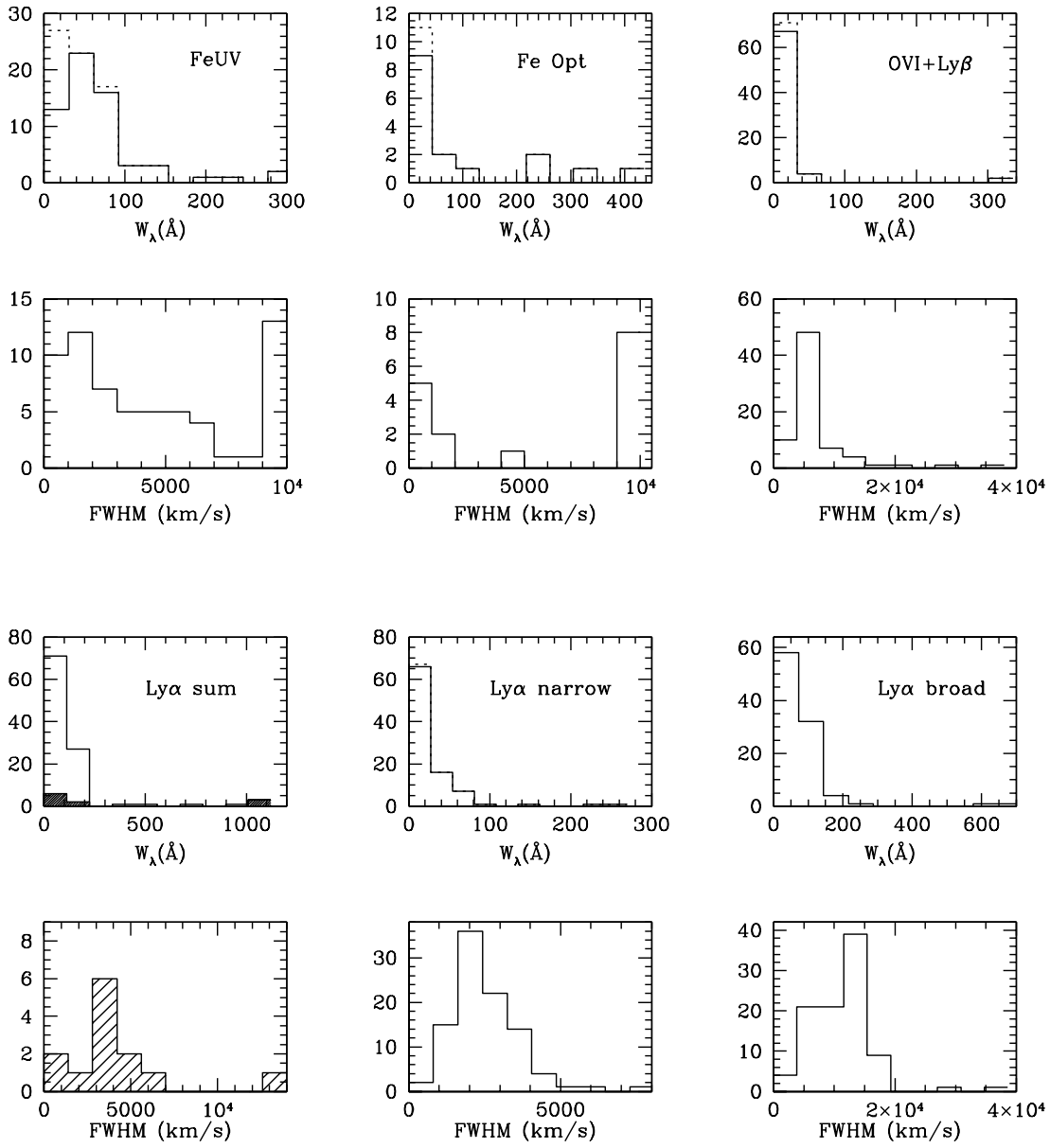

FIG. 2.—Distribution of rest-frame W_λ (*top and third row*) and FWHM (*second from top and bottom row*) of the emission line properties of AGNs in the post-COSTAR FOS sample. When upper limits in W_λ are present, we show the estimated Kaplan-Meier distributions with a dashed line. Shaded areas represent distributions for the single Gaussian components of the strong emission lines: Lyα, C IV, C III], and Mg II.

were obtained by excluding off-nuclear spectra (e.g., the 10 different NLR knots of Mrk 78). To avoid excessive weight given to a single object, in cases of multiple spectra we tally only measurements from the spectrum with the highest S/N and resolution. In total 1607 emission lines have been modeled among which 97 are upper limits. In Table 5 the name of the emission line is given in column (1), followed by the total number of emission lines modeled (col. [2]) and the number of upper limits (col. [3]). The mean, standard deviation and median of the W_λ and FWHM for the detected lines are presented in columns (4)–(6) and (10)–(12), respectively. When upper limits in W_λ were present we used the nonparametric survival analysis technique and a Kaplan-Meier estimator to reconstruct the true W_λ distribution and to calculate the means and medians in columns (7)–(8) (for reference, see Isobe, Feigelson, & Nelson 1986 and Lavalley, Isobe, & Feigelson 1992).

Since the strong emission lines such as Lyα, C IV, C III], Mg II, Hβ, and Hα were fitted using either two (broad and narrow) components or one (single) component, we calculated the W_λ and FWHM means and medians for these components separately. The mean and median W_λ for the whole line (indicated as the "Sum" in Table 5) was calculated as either the sum of the broad and narrow components or the single component alone.

Both the pre- and post-COSTAR FOS samples are heterogeneous, and represent neither complete nor uniform selection. Nevertheless, as a check on our methods and on the consistency between these samples we compare the statistical properties of the W_λ and FWHM of the pre-COSTAR sample analyzed in Paper II and the post-COSTAR sample presented here. Overall, the means and medians for the UV lines agree within the errors. We did not, however, attempt to compare the W_λ of post-COSTAR single components of the strong

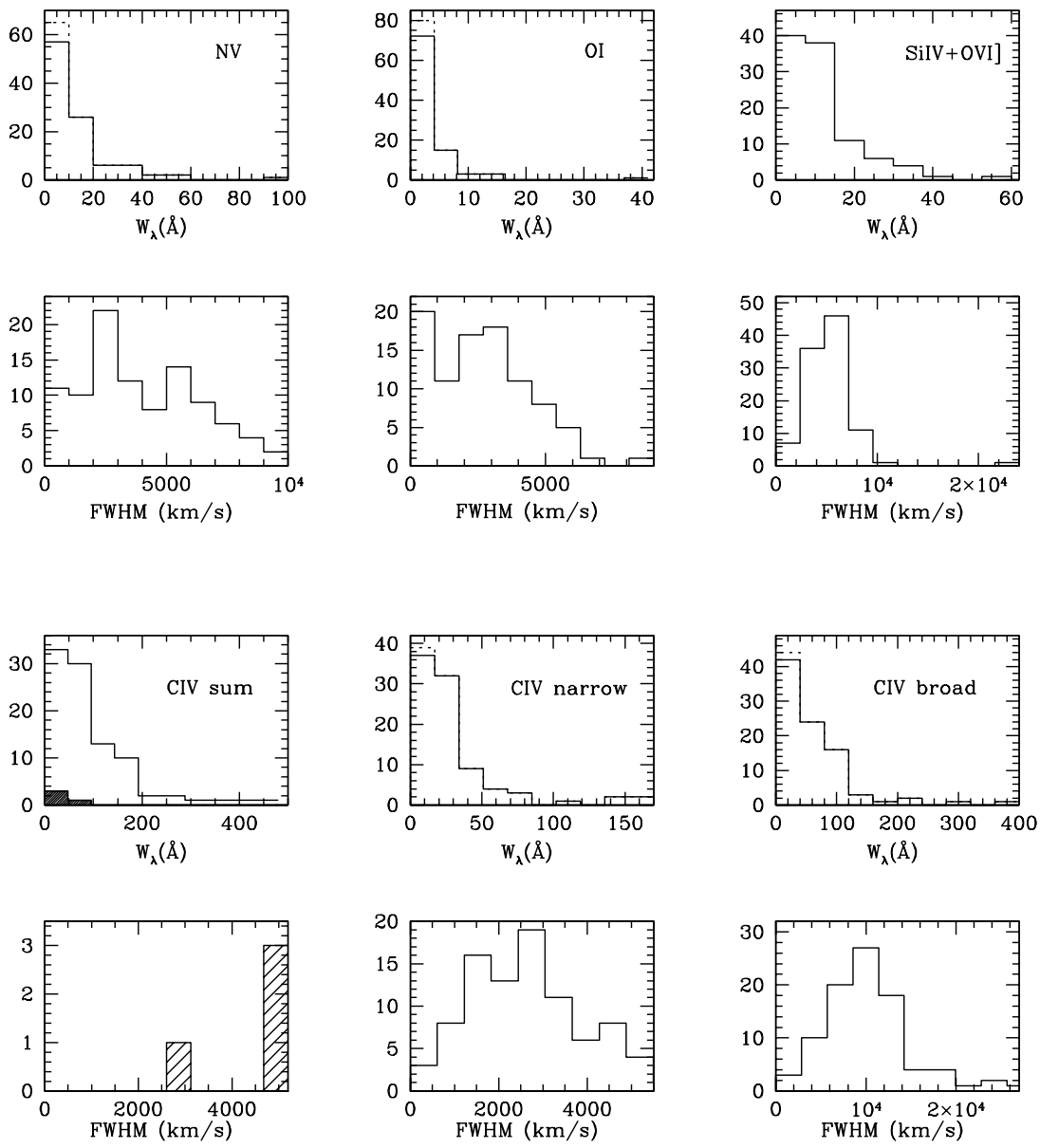

FIG. 2.—*Continued*

emission lines or optical lines redward of Ne V with the pre-COSTAR sample measurements, since the number of available W_λ in both or either samples is too small for meaningful analysis.

Histograms of W_λ and FWHM of the emission lines blueward of Mg II are presented in Figure 2. The first and third rows represent the W_λ distributions, while the second and fourth rows give the FWHM distributions. In all panels, solid lines represent distributions for detections, while the dotted lines show the estimated W_λ distributions from the Kaplan-Meier estimator if upper limits are present. In the panels that show the sum of Lyα, C IV, C III], and Mg II distributions, the shaded histograms represent results from single Gaussian component fits.

The luminosity and redshift range of the post-COSTAR sample is comparable to the pre-COSTAR sample analyzed in Paper II (see Fig. 3). However, the post-COSTAR sample shows a larger number of low-luminosity AGNs such as Seyferts, LINERs, and NLS1s. Objects with log $L(2500\ \text{Å}) < 30$ comprise of $\sim$30% of the post-COSTAR sample and only 15% of the pre-COSTAR sample. In Figure 4 we show the distributions of log $L(2500$ Å) for both samples. The two-tailed Kolmogorov-Smirnow test gave a 99.9% probability that these distributions are different.

6. CONCLUSIONS

We have presented the emission line measurements of a sample of AGNs that has been observed by the *HST* FOS after the installation of COSTAR. Our sample includes 180 objects and 220 spectra, which have been modeled using an automated technique that fits multiple Gaussians to the emission lines, taking into account Galactic reddening, blended iron emission, and Galactic and intrinsic absorption lines. In this paper we present uniform measurements of 1607 emission lines including equivalent widths, FWHM, and shifts from the line's expected position and calculate upper limits for weak lines. We also present the underlying continuum parameters (slopes and normalization). This is the third paper

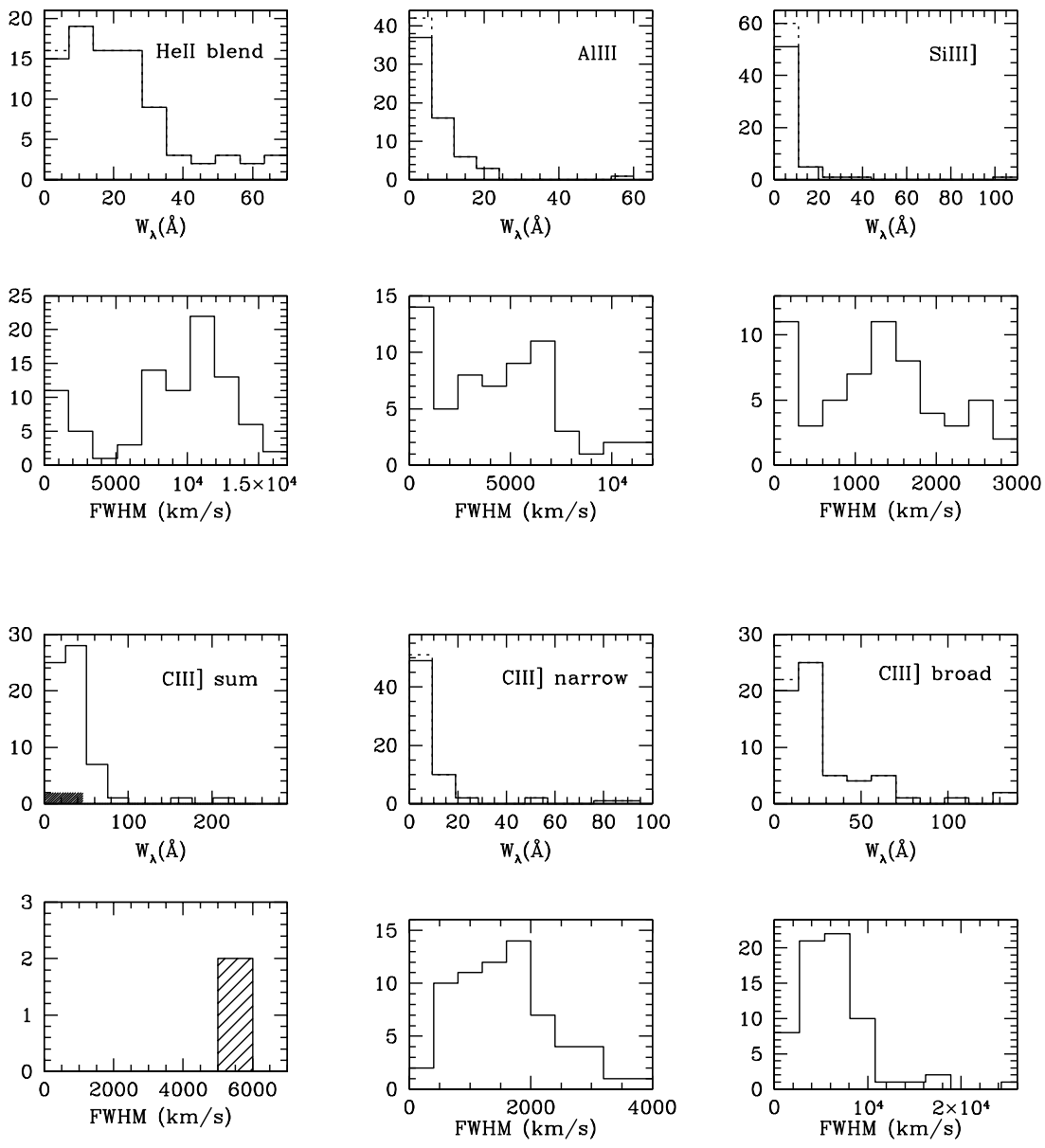

FIG. 2.—*Continued*

in a series of papers aimed at uniformly measuring emission line properties in large AGN samples. It has been preceded by a presentation of emission line properties in ~1000 optical spectra from the Large Bright Quasar Survey (Paper I) and ~200 UV spectra observed by *HST* FOS in the pre-COSTAR era (Paper II). All 1387 spectral fits and tabulated results are available at our Web site (see footnote 3). Such large uniformly measured databases will hopefully bring us closer to a better understanding of the origin of the line emitting regions and their relationship to the central engine.

P. J. G. and J. K. gratefully acknowledge support provided by NASA through grant NAG5-6410 (LTSA). P. J. G. and T. A. acknowledges support through NASA contract NAS8-39073 (CXC). M. V. acknowledges financial support for Proposal number AR-09549, provided by NASA through a grant from the Space Telescope Science Institute, which is operated by the Association of Universities for Research in Astronomy, Inc., under NASA contract NAS5-26555. We are grateful to Todd Boroson for providing the Fe II optical template. This research was made based on observations made with the NASA/ESA *Hubble Space Telescope*, obtained from the data archive at the Space Telescope Science Institute and using the Multimission Archive at the Space Telescope Science Institute (MAST). STScI is operated by the Association of Universities for Research in Astronomy, Inc., under NASA contract NAS5-26555. Support for MAST for non-*HST* data is provided by the NASA Office of Space Science via grant NAG5-7584 and by other grants and contracts. This research has also made use of the NASA/IPAC Extragalactic Database (NED), which is operated by the Jet Propulsion Laboratory, California Institute of Technology, under contract with the National Aeronautics and Space Administration.

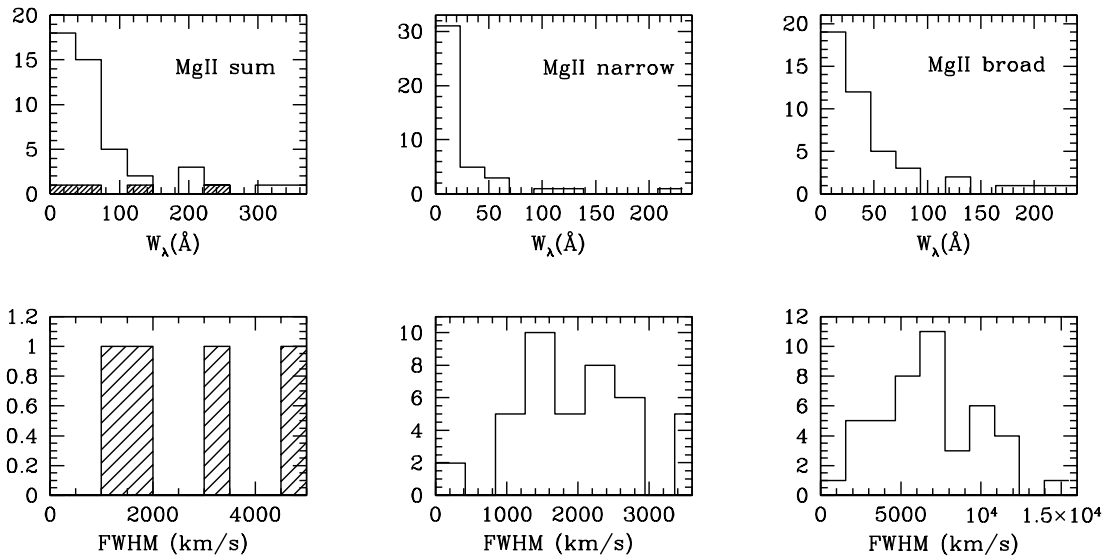

FIG. 2.—*Continued*

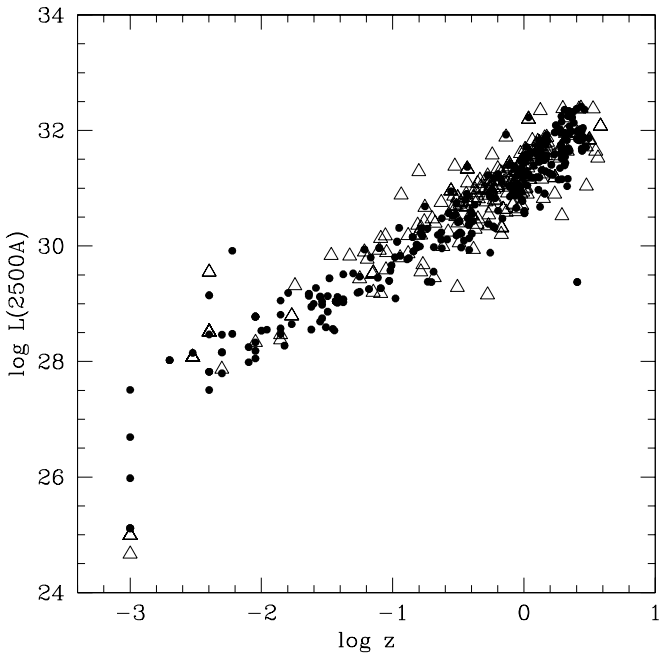

FIG. 3.—Luminosity at 2500 Å vs. redshift for the post-COSTAR sample analyzed here (*filled circles*) and the pre-COSTAR sample analyzed in Paper II (*open triangles*).

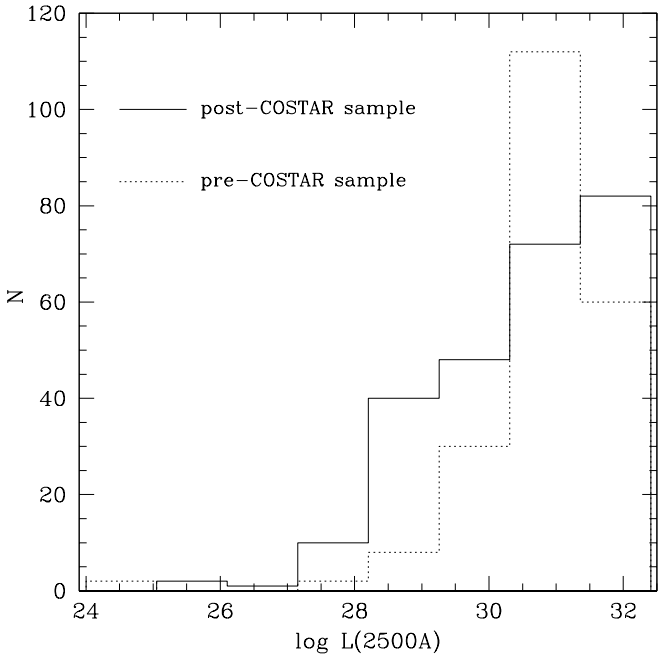

FIG. 4.—Distribution of luminosity at 2500 Å for AGNs from the post-COSTAR sample (*solid line*) and the pre-COSTAR sample (*dotted line*). The two distributions are different at the 99.9% level with post-COSTAR sample having a higher percentage of low-luminosity [log $L(2500) < 30$] objects.

APPENDIX

NOTES ON INDIVIDUAL OBJECTS

0039−5117oa.—Two power-law continua were fitted to this spectrum, which were joined at a nonstandard wavelength of 3000 Å observed frame, for a better continuum fit.

0238+1636oa.—This BL Lac object is included in our sample as it shows weak emission lines.

0241−0815oa.—Spectrum spans a large wavelength range from 2200 to 6800 Å, so the power-law continuum does not fit the spectrum well, especially at Hα wavelengths.

0320−1926oa, 1337+2423oa, 1959+4044oa.—Short spectra with only one standard continuum window; for a better continuum fit we added a nonstandard continuum window at red side of Mg II.

0742+6510oa–oj.—Spectra of 10 different NLR knots in Mrk 78 (a Seyfert 2) showing interaction of the NLR gas with the ISM.

1048−2509oa.—Very weak continuum.

1223+1545oa.—Very weak continuum.

1252+2913oa.—Used a nonstandard continuum window at wavelengths 2100–2130 Å observed frame.

1719+4858oa.—Missing spectrum at C IV wavelengths.

1842+7946oa.—Missing spectrum at C IV wavelengths.

1902+3159oa.—Added additional window blue of Lyα for better continuum fit.

1927+7358oa.—Missing spectrum at Lyα wavelengths.

REFERENCES

Aldcroft, T. A. 1993, Ph.D. thesis, Stanford Univ.
Baldwin, J. A. 1977, ApJ, 214, 679
Baldwin, J. A., Burke, W. L., Gaskell, C. M., & Wampler, E. J. 1978, Nature, 273, 431
Baldwin, J. A., Ferland, G., Korista, K., & Verner, D. 1995, ApJ, 455, L119
Boroson, T. A. 2002, ApJ, 565, 78
Boroson, T. A., & Green, R. F. 1992, ApJS, 80, 109
Brandt, N., & Boller, Th. 1998, Astron. Nachr., 319, 163
Brotherton, M. S., Wills, B. J., Francis, P. J., & Steidel, C. C. 1994, ApJ, 430, 495
Cardelli, J. A., Clayton, G. C., & Mathis, J. S. 1989, ApJ, 345, 245
Corbin, M. R., & Boroson, T. A. 1996, ApJS, 107, 69
Dietrich, M., Hamann, F., Shields, J. C., Constantin, A., Vestergaard, M., Chaffee, F., Foltz, C. B., & Junkkarinen, V. T. 2002, ApJ, 581, 912
Elvis, M. 2000, ApJ, 545, 63
Elvis, M., Wilkes, B. J., & Lockman, F. J. 1989, AJ, 97, 77
Forster, K., Green, P. J., Aldcroft, T., Vestergaard, M., & Foltz, C. B. 2001, ApJS, 134, 35 (Paper I)
Freeman, P. Doe, S., & Siemiginowska, A. 2001, Proc. SPIE, 4477, 76
Ganguly, R., Bond, N. A., Charlton, J. C., Eracleous, M., Brandt, W. N., & Churchill, C. W. 2001, ApJ, 549, 133
Gehrels, N. 1986, ApJ, 303, 336
Green, P. J. 1998, ApJ, 498, 170
Green, P. J., Forster, K., & Kuraszkiewicz, J. K. 2001, ApJ, 556, 727
Heiles, C., & Cleary, M. N. 1979, Australian J. Phys. Astrophys. Suppl., 47, 1
Isobe, T., Feigelson, E. D., & Nelson, P. I. 1986, ApJ, 306, 490
Keyes, C. D., Koratkar, A. P., Dahlem, M., Hayes, J., Christiansen, J., & Martin, S. 1995, Faint Object Spectrograph Instrument Handbook, version 6.0 (Baltimore: STScI)
Kinney, A. L., Rivolo, A. R., & Koratkar, A. P. 1990, ApJ, 357, 338
Kuraszkiewicz, J. K., Green, P. J., Forster, K., Aldcroft, T. L., Evans, I. N., & Koratkar, A. 2002, ApJS, 143, 257 (Paper II)
Laor, A., & Brandt, W. N. 2002, ApJ, 569, 641
Laor, A., Fiore, F., Elvis, M., Wilkes, B., & McDowell, J. C. 1997, ApJ, 477, 93
Lavalley, M., Isobe, T., & Feigelson, E. D. 1992, in ASP Conf. Ser. 25, Astronomical Data Analysis Sortware and Systems I, ed. D. M. Woarral, C., Biemsderfer, & J. Barnes (San Francsico: ASP), 245
Lockman, F. J., & Savage, B. D. 1995, ApJS, 97, 1
Marziani, P., Sulentic, J. W., Dultzin-Hacyan, D., Calvani, M., & Moles, M. 1996, ApJS, 104, 37
Murray, N., & Chiang, J. 1995, ApJ, 454, L105
Netzer, H., Laor, A., & Gondhalekar, P. M. 1992, MNRAS, 254, 15
Shang, Z., Wills, B. J., Robinson, E. L., Wills, D., Laor, A., Xie, B., & Yuan, J. 2003, ApJ, 586, 52
Stark, A. A., Gammie, C. F., Wilson, R. W., Bally, J., Linke, R. A., Heiles, C., & Hurwitz, M. 1992, ApJS, 79, 77
Steidel, C. C., & Sargent, W. L. W. 1991, ApJ, 382, 433
Sulentic, J. W., Zwitter, T., Marziani, P., & Dultzin-Hacyan, D. 2000, ApJ, 536, L5
Veron-Cetty, M.-P., & Veron, P. 1996, Catalog of Quasars and Active Galactic Nuclei (7th ed.; Garching: ESO)
Vestergaard, M., & Wilkes, B. J. 2001, ApJS, 134, 1
Wampler, E. J., Gaskell, C. M., Burke, W. L., & Baldwin, J. A. 1984, ApJ, 276, 403
Wang, T.-G., Lu, Y.-J., & Zhou, Y.-Y. 1998, ApJ, 493, 1
Wilkes, B. J., Kuraszkiewicz, J., Green, P. J., Mathur, S., & McDowell, J. C. 1999, ApJ, 513, 76
Wills, B. J., Laor, A., Brotherton, M. S., Wills, D., Wilkes, B. J., Ferland, G. J., & Shang, Z. 1999, ApJ, 515, L53
Wills, B. J., Netzer, H., & Wills, D. 1985, ApJ, 288, 9
Wu, C.-C., Boggess, A., & Gull, T. R. 1983, ApJ, 266, 28
Yuan, W., Siebert, J., & Brinkmann, W. 1998, A&A, 334, 498
Zamorani, G., Marano, B., Mignoli, M., Zitelli, V., & Boyle, B. J. 1992, MNRAS, 256, 238
Zheng, W., & Malkan, M. A. 1993, ApJ, 415, 517